THE JOURNAL OF BIOLOGICAL CHEMISTRY VOL. 290, NO. 5, pp. 2644–2658, January 30, 2015

Structural Model of the Cytosolic Domain of the Plant Ethylene Receptor 1 (ETR1)

Received for publication, June 10, 2014, and in revised form, November 24, 2014 Published, JBC Papers in Press, December 1, 2014, DOI 10.1074/jbc.M114.587667

Hubert Mayerhofer[1], **Saravanan Panneerselvam**[2], **Heidi Kaljunen, Anne Tuukkanen**[3], **Haydyn D. T. Mertens**[3], **and Jochen Mueller-Dieckmann**[4]

From the European Molecular Biology Laboratory (EMBL) Hamburg, c/o Deutsches Elektronen-Synchrotron (DESY), Building 25A, Notkestrasse 85, 22603 Hamburg, Germany

Background: Signaling of the phytohormone ethylene is initiated by ethylene receptors.
Results: We present two crystal structures and a solution model of the entire cytosolic domain of ETR1.
Conclusion: This first structural model of the cytosolic domains reveals a flexible receiver domain and asymmetry of the central dimerization domain.
Significance: The molecular architecture of the isolated cytosolic domain forms the basis to understand receptor assembly and interaction.

Ethylene initiates important aspects of plant growth and development through disulfide-linked receptor dimers located in the endoplasmic reticulum. The receptors feature a small transmembrane, ethylene binding domain followed by a large cytosolic domain, which serves as a scaffold for the assembly of large molecular weight complexes of different ethylene receptors and other cellular participants of the ethylene signaling pathway. Here we report the crystallographic structures of the ethylene receptor 1 (ETR1) catalytic ATP-binding and the ethylene response sensor 1 dimerization histidine phosphotransfer (DHp) domains and the solution structure of the entire cytosolic domain of ETR1, all from *Arabidopsis thaliana*. The isolated dimeric ethylene response sensor 1 DHp domain is asymmetric, the result of different helical bending angles close to the conserved His residue. The structures of the catalytic ATP-binding, DHp, and receiver domains of ethylene receptors and of a homologous, but dissimilar, GAF domain were refined against experimental small angle x-ray scattering data, leading to a structural model of the entire cytosolic domain of the ethylene receptor 1. The model illustrates that the cytosolic domain is shaped like a dumbbell and that the receiver domain is flexible and assumes a position different from those observed in prokaryotic histidine kinases. Furthermore the cytosolic domain of ETR1 plays a key role, interacting with all other receptors and several participants of the ethylene signaling pathway. Our model, therefore, provides the first step toward a detailed understanding of the molecular mechanics of this important signal transduction process in plants.

Ethylene acts as a phytohormone that controls numerous aspects of plant growth and development. In *Arabidopsis thaliana*, the many responses to ethylene are initiated by a group of five membrane-bound receptors (ETR1,[5] ETR2, ERS1, ERS2, and EIN4) (1). The basic functional unit of the receptors is a disulfide-linked dimer (2), which binds one copper ion and therefore one ethylene (3). In contrast to the majority of membrane receptors, ethylene receptors lack a soluble signal binding domain. Instead, ethylene binds at the dimer interface of the conserved hydrophobic N-terminal receptor domain (4), which is embedded in the membrane of the endoplasmic reticulum (5) and directly controls the activity of its cytosolic domain.

Ethylene receptors are part of high molecular mass multiple protein complexes when isolated from *A. thaliana* membranes (6). To this end, the C-terminal cytosolic receptor domain serves as a docking station for many cellular components, which directly or indirectly contribute to signal transduction. The cytosolic domain itself comprises a GAF (cGMP-specific phosphodiesterase, adenylyl cyclases, and FhlA) domain followed by an HK and in some instances (ETR1, ETR2, and EIN4) a receiver domain. The histidine kinase and receiver domains resemble classical bacterial two-component systems. In prokaryotes, they constitute a phosphoryl relay, which regulates numerous signaling pathways by subsequently executing autokinase, phosphotransferase, and phosphatase reactions (7). Ethylene receptors were the first example of two-component system-like signaling modules discovered in eukaryotes (8). Although ETR1 and ERS1, which constitute subfamily 1, possess all of the conserved hallmark residues associated with HK activity, members of subfamily 2 (ETR2, ERS2, and EIN4) lack one or more of those residues. Consistent with this discovery,

The atomic coordinates and structure factors (codes 4MTX, 4MT8, and 4PL9) have been deposited in the Protein Data Bank (http://wwpdb.org/).

[1] Present address: Inst. de Biologie Structurale, UMR5075 CEA-CNRS-Université Joseph Fourier Grenoble 1, 71 avenue des Martyrs, 38044 Grenoble, France.
[2] Present address: HASYLAB, DESY, Bldg. 25F, Notkestrasse 85, 22603 Hamburg, Germany.
[3] Supported by fellowships from the EMBL Interdisciplinary Postdocs program.
[4] To whom correspondence should be addressed: Abteilung für Mikrobiologie und Biotechnologie, Biozentrum Klein Flottbek, Universität Hamburg, Ohnhorststrasse 18, 22609 Hamburg, Germany. Tel.: 49-40-42816-651; Fax: 49-40-42816-459; E-mail: jochen.mueller-dieckmann@uni-hamburg.de.

[5] The abbreviations used are: ETR, ethylene receptor; CA, catalytic ATP-binding; CTR1, constitutive triple response-1; DHp, dimerization histidine phosphotransfer; ERS, ethylene response sensor; HK, histidine kinase; NDSB, 3-(1-pyridinio)-1-propanesulfonate; RD, receiver domain; SAXS, small angle x-ray scattering; GAF, cGMP-specific phosphodiesterase, adenylyl cyclases, and FhlA; res., residues; Ni-NTA, nickel-nitrilotriacetic acid; SAD, single-wavelength anomalous diffraction; MM, molecular mass; SG, space group; r.m.s.d, root mean square deviation; AMPPNP, adenosine 5′-(β,γ-imino)triphosphate.

histidine autophosphorylation of ETR1 and ERS1 was demonstrated *in vitro* (9, 10). This activity, however, appears not to be essential for *in vivo* signaling (11). Subfamily 2 receptors and ERS1 show Ser/Thr kinase activity (10). Although all receptors contribute to ethylene signaling (12), subfamily 1 receptors play a prominent role. For instance, the effect of silver, an ethylene antagonist, was shown to mostly depend on ETR1 (13).

The relevance of the GAF domain for ethylene signaling remains unknown. The histidine kinase can be subdivided into a dimerization and a catalytic domain. The conserved, phosphoryl-accepting His is located in the dimerization domain DHp. The catalytic domain binds the phosphoryl donor ATP. At present, only structures of prokaryotic HK domains, mainly of the individual domains, are available. More recently the complex between an HK domain and its separate cognate receiver domain from *Thermotoga maritima* (14) and the complete cytoplasmic region of VicK (15) from *Streptococcus mutans* have been determined. Depending on the functional state of the receptor, the interaction and relative orientations of the DHp and CA domains vary (14, 16). The phosphatase-competent state was suggested to display the tightest interaction and closest conformation. In the other two states, phosphotransferase and autokinase, the DHp-CA domain interaction weakens: the CA domain position is more flexible, and the DHp domain exhibits varying degrees of intramolecular asymmetry displayed by different conformations of its N-terminal helices (15–17).

In contrast to canonical prokaryotic two-component systems, ethylene receptors control the activity of a cytosolic protein kinase, CTR1 (18, 19). In the absence of ethylene, both receptor and CTR1 are active. Complex formation of ethylene receptors and CTR1 was shown *in vivo* (19). It involves parts of the HK and RD domains on the ethylene receptor and the N-terminal domain of CTR1 (18–20). CTR1 is homologous to the family of rapidly accelerated fibrosarcoma kinases (21), but no definite proof of an associated canonical MAPK cascade exists (22, 23). More recently EIN2 was shown to be a substrate of CTR1 activity. Phosphorylation of EIN2 by CTR1 prevents its activation and the transport of its cytosolic C-terminal domain into the nucleus (24, 25). Consequently ethylene signaling in plants combines signal transduction elements from prokaryotic and eukaryotic backgrounds. Ethylene-induced conformational changes within the cytosolic domain are thought to translate into conformational changes within CTR1 and thereby manipulate the initial steps of intracellular signal transduction. This step in the signal transduction is still not well understood and relies on evidence from mutants and studies on the subcellular location of CTR1 (18, 19, 26).

In addition to the basic functional homodimer, non-covalent higher order complexes between ethylene receptors have been discovered (6, 27). They provide a plausible explanation for the broad range of ethylene sensitivity (0.2 nl–1,000 μl/liter) as well as the dominant nature of ethylene-insensitive mutants. The functional basis of these inter-receptor signaling networks has only just begun to emerge (28). Recently a signaling pathway relying only on the N-terminal part of ETR1 (res. 1–349), which acts independently of CTR1 but can be inhibited by it (29), was described. This observation adds to the complexity of ethylene receptor signaling.

Here we present the crystallographic structures of the DHp domain of ERS1 (DHp^{ERS1}; res. 308–407; 84% identical with ETR1 equivalent), the CA domain of ETR1 (CA^{ETR1}; res. 407–589) bound to ADP, and the solution structure of the entire cytosolic domain of ETR1 lacking the transmembrane domain (ETR1-ΔTM; res. 158–738). Crystallographic models of a homologous GAF domain (Protein Data Bank code 2O9B (30)), DHp^{ERS1} and CA^{ETR1} of this report, and the receiver domain from a previous study (RD^{ETR1}) (31) were used as input rigid bodies and refined against the SAXS data of the entire cytosolic domain. They provide the first model of the entire intracellular receptor domain of this important class of plant hormone signal transducers. In addition, the isolated DHp^{ERS1} domain exhibits an interesting asymmetry that likely represents the ground state of the central part of the receptor.

EXPERIMENTAL PROCEDURES

Protein Expression and Purification: Cloning and Purification of ETR1-ΔTM

N-terminally His-tagged ETR1-ΔTM (res. 158–738) was amplified from a cDNA library obtained from the *Arabidopsis* Biological Research Centre at Ohio State University (21). The PCR protocol consisted of 25 cycles of annealing at 336 K followed by 10 s of extension at 345 K using *Thermococcus kodakarensis* polymerase (Novagen). The sequences of the forward and reverse primers were 5′-CAGGGCGCCAGTGATAGACACTATTTTAAAGACTACACTTGTTGAGC-3′ and 5′-GACCCGACGCGGTTACATGCCCTCGTACAGTACCCG-3′, respectively.

Both primers contain appropriate extensions for ligation-independent cloning. The gene was inserted via ligation-independent cloning into a modified pETM-11/LIC vector where the N-terminal hexa-His tag is followed by a GB1 expression and solubility enhancer (32) and a tobacco etch virus site. The final inserts were verified by DNA sequencing. The protein was expressed in *Escherichia coli* Rosetta cells in 2 liters of terrific broth medium. Cells were grown to an A_{600} of 1.5, cooled to 20 °C, induced with 0.05 mM isopropyl 1-thio-β-D-galactopyranoside, and harvested after 18 h. The cells were lysed in 20 mM Tris, pH 8.8, 150 mM NaCl, 1 M urea, 3 mM β-mercaptoethanol, 0.1% (w/v) CHAPS (Carl Roth, Germany), 20 mM imidazole, EDTA-free protease inhibitors (cOmplete ULTRA Tablets, Mini, Roche Applied Science), and 10 μg ml^{-1} DNase. The Ni-NTA purification steps were carried out as described for $ERS1^{DHP}$ (33) with the exception of adding 0.1% (w/v) CHAPS to the Ni-NTA wash buffer and dialyzing pooled fractions against 30 mM Tris, pH 8.8, 100 mM NaCl, 6 mM β-mercaptoethanol, and 3% glycerol during the tobacco etch virus digestion step at 4 °C for 18 h. After the second Ni-NTA step, the sample was either used directly for SAXS measurements (no NDSB 201 added; see Fig. 6*B*), or NDSB 201 was added, and size exclusion chromatography (HiLoad 26/60 Superdex 200, Amersham Biosciences) was used as the final purification step. The column was pre-equilibrated in 20 mM Tris, pH 8.8, 150 mM NaCl, 1 mM DTT, and 250 mM NDSB 201. ETR1-ΔTM was concentrated

TABLE 1

Refinement and model quality statistics of DHp^{ERS1} and CA^{ETR1}, respectively

Statistics for the highest resolution shell are shown in parentheses. r.m.s., root mean square.

Protein	DHp^{ERS1}	DHp^{ERS1}	CA^{ETR1}
Space group	$C222_1$	$P2_12_12$	$I2_12_12_1$
Resolution (Å)	1.90	2.15	1.90
R_{work}	0.1948 (0.2872)	0.1984 (0.2373)	0.1469 (0.1380)
R_{free}	0.2265 (0.4067)	0.2506 (0.3133)	0.1822 (0.2103)
Number of atoms	1634	3224	2606
Macromolecules	1550	3048	1182
Water	84	176	99
r.m.s. bonds (Å)	0.017	0.011	0.010
r.m.s. angles (°)	1.48	1.28	1.34
Ramachandran favored (%)	99	100	99
Ramachandran outliers (%)	0	0	0
Clash score	5.81	9.42	23.63
Average B-factor	36.90	33.10	41.80
Macromolecules	36.90	33.00	40.90
Solvent	37.40	35.30	50.70

TABLE 2

Data collection statistics of DHp^{ERS1} Se-Met crystals

Statistics for the highest resolution shell are shown in parentheses.

	Se-Met peak	Se-Met inflection
X-ray source	X12, DESY	X12, DESY
Wavelength (Å)	0.9772	0.9777
Resolution range (Å)	47.3–3.0 (3.15–3.0)	47.3–3.0 (3.15–3.0)
Temperature (K)	100	100
Crystal-to-detector distance (mm)	272	272
Rotation range per image (°)	1.1	1.1
Total rotation range (°)	154	154
Space group	$C222_1$	$C222_1$
Cell dimensions (Å)	$a = 75.20$, $b = 99.09$, $c = 77.12$	$a = 75.16$, $b = 99.07$, $c = 77.09$
Observed reflections	36,987 (5,733)	36,764 (5,768)
Unique reflections	11,119 (1,743)	11,090 (1,755)
Multiplicity	3.3 (3.3)	3.3 (3.3)
R_{merge} (%)	7.0 (26.0)	7.3 (27.5)
R_{pim} (%)	4.6 (17.1)	4.8 (18.1)
Completeness (%)	99.8 (99.1)	99.9 (99.6)
$I/\sigma(I)$	17.6 (6.1)	16.8 (5.4)

using a Vivaspin concentrator (30,000 molecular weight cutoff, Vivascience, Germany).

X-ray Structure Determination

Structure Determination of DHp^{ERS1}—Cloning, expression, purification, and crystallization of the DHp domain of ERS1 (DHp^{ERS1}, $ERS1^{308-407}$) have been described previously (33). The structure of DHp^{ERS1} was solved using the peak and inflection point data sets of an Se-Met crystal collected on beamline X12 (EMBL-Hamburg, DESY). The crystal was rotated in steps of 1.1° over a total range of 154°. Data were processed with XDS (34) and scaled with SCALA (35, 36). Phases were obtained using HKL2MAP (37), and an initial model was built into the resulting experimental electron density map using ARP/wARP (38). The model was refined against native 1.9-Å data in $C222_1$ and 2.15-Å data in $P2_12_12$, both collected on beamline ID29 at the European Synchrotron Radiation Facility, Grenoble, France. Iterative cycles of PHENIX (39) were followed by manual model building in Coot (40). Non-crystallographic symmetries were excluded from the refinement due to structural differences in the individual monomers. MolProbity (41) analysis indicated that the overall geometry of the final model ranked in the 98th percentile (MolProbity score of 1.38) for $C222_1$ and in the 99th percentile (MolProbity score of 1.43) for $P2_12_12$ where the 100th percentile is best among structures of comparable resolution. Figures were generated using the PyMOL Molecular Graphics System, Version 1.5.0.4, Schrödinger, LLC. The statistics of the x-ray diffraction data sets and structure refinement are summarized in Tables 1 and 2.

Structure Determination of CA^{ETR1}—Cloning, expression, purification, and crystallization of CA^{ETR1} (residues 407–589) have been described previously (42). A native data set was collected at beamline PX III of the Swiss Light Source at a wavelength of 0.998 Å. The structure was solved by molecular replacement with the CA domain of HK853 (Protein Data Bank code 2C2A) as a search template using Auto-Rickshaw (43). The model was manually corrected with Coot (40) and refined with PHENIX (39). To confirm the identity of metal ions in the structure, SAD data were collected to a resolution of 2.2 Å at beamline X12 (EMBL-Hamburg, DESY) and a wavelength of 1.377 Å. Phases were independently calculated with the SAD phasing protocol of the Auto-Rickshaw web server (43) and by using the SHELXD/E program suite (44). Initial phases were further improved with the MRSAD protocol of Auto-Rickshaw (43). The statistics of data collection and structure refinement are given in Table 1.

SAXS Experiments

SAXS measurements were carried out at beamline P12 (EMBL-Hamburg, DESY) at the PETRA-III storage ring using a Pilatus 2M detector (Dectris) and at the X33 beamline (EMBL-Hamburg, DESY) at the DORIS storage ring using a Pilatus 1M detector (45). The purified ETR1-ΔTM receptor domain was measured at several concentrations (0.3–1.4 mg/ml). Concentrations were determined by measuring the absorption at 280 nm using a NanoDrop ND-1000 spectrophotometer (NanoDrop Technologies, Wilmington, DE), and an absorption of 0.502 (at a concentration of 0.1% (=1 g liter^{-1}) at 280 nm) was determined. For each measurement, 20 50-ms frames were collected and averaged using a sample volume of 30 μl at a temperature of 10 °C. The SAXS camera was set to a sample-detector distance of 3.1 m, covering the momentum transfer range $0.008\ Å^{-1} < s < 0.47\ Å^{-1}$ ($s = 4\pi \sin(\theta)/\lambda$ where 2θ is the scattering angle and $\lambda = 1.24$ Å is the x-ray wavelength). Prior to and following each sample exposure, the buffer excluding the protein was measured to allow for background subtraction.

The data were corrected for buffer contribution, scaled for solute concentration, and extrapolated to infinite dilution using the program PRIMUS (46). The radius of gyration (R_g) and forward scattering intensity $I(0)$ were determined using Guinier analysis (47) assuming that at very small angles ($s \leq 1.3/R_g$) the intensity is represented as $I(s) = I(0)\exp((sR_g)^2/3)$. R_g and $I(0)$ were also independently determined along with the maximum particle dimension (D_{max}) using the indirect Fourier transformation approach in the program GNOM (48). The molecular mass (MM_{SAXS}) of the construct was calculated by comparison of the extrapolated forward scattering with reference BSA samples (66 kDa). The excluded volume of the hydrated particle (V_p) was computed from the small angle portion of the data ($s < 0.25\ Å^{-1}$) using DATPOROD (49), and an estimate of MM was also extracted. For globular proteins, Porod volumes in Å^3 are about 1.7 times the molecular masses in Da (49). The scattering

TABLE 3
SAXS data collection and scattering-derived parameters

Data collection parameters		
	ETR1-ΔTM	**ETR1-ΔTM + NDSB**
Instrument	P12-EMBL (storage ring PETRAIII, Hamburg, Germany)	X33-EMBL (storage ring DORIS-III, Hamburg, Germany)
Beam geometry (mm^2)	0.2 x 0.12	2.0 x 0.6
Wavelength (Å)	1.24	1.54
s-range ($Å^{-1}$)	0.008 – 0.47	0.01 - 0.6
Exposure time (ms)	1 (20 x 0.05)	120 (8 x 15)
Concentration range (mg ml^{-1})	0.7 - 4.2	0.7 – 2.7
Temperature (K)	283	283
*Structural parameters**		
$I(0)$ (arbitrary units) (from $P(r)$)	1175 ±10	72.5 ± 0.3
R_g (Å) (from $P(r)$)	59 ± 6	48.8 ± 1
$I(0)$ (arbitrary units) (from Guinier)	1164 ± 40	67.9 ± 0.7
R_g (Å) (from Guinier)	55 ± 11	47.9 ± 2
D_{max} (Å)	190 ± 5	150 ± 5
Porod volume estimate ($Å^3$)	274000 ± 4200	289000 ± 5000
Dry volume calculated from sequence ($Å^3$)	78367	78367
*Molecular mass determination**		
Contrast ($\Delta\rho$ x 10^{10} cm^{-2})	3.047	2.610
Molecular mass M_r (from $I(0)$)	53000 ± 5000	55310 ± 5000
Molecular mass M_r (from Porod volume)	161200 ± 24000	169886 ± 20000
Calculated monomeric M_r from sequence	64771.3	64771.3
Software employed		
Primary data reduction	Automated radial averaging (65)	
Data processing	*PRIMUS*	
Ab initio analysis	*DAMMIN*	
Validation and averaging	*DAMAVER*	
Rigid body modelling	*CORAL, EOM*	
Computation of model intensities	*CRYSOL*	
3D graphics representations	*PYMOL*	

*, reported for 0.66 mg ml^{-1} measurement.

TABLE 4
SAXS data collection and scattering-derived parameters for short ETR1-ΔTM constructs

Data collection parameters		
	$ETR1^{DHp-CA-RD}$	**$ETR1^{DHp-CA}$**
Instrument	X33-EMBL (storage ring DORIS-III, Hamburg, Germany)	
Beam geometry (mm)	2.0 x 0.6 mm^2	2.0 x 0.6 mm^2
Wavelength (Å)	1.54	1.54
s-range ($Å^{-1}$)	0.01 – 0.6	0.01 – 0.6
Exposure time (s)	120 (8 x 15)	120 (8 x 15)
Concentration range (mg ml^{-1})	0.7 – 5.0	0.6 – 6.0
Temperature (K)	283	283
*Structural parameters**		
$I(0)$ (arbitrary units) (from $P(r)$)	63.7 ± 5	22.1 ± 0.3
R_g (Å) (from $P(r)$)	41.1 ± 1	27.6 ± 1
$I(0)$ (arbitrary units) (from Guinier)	63.6 ± 1	22.2 ± 1
R_g (Å) (from Guinier)	39.8 ± 1	29.4 ± 2
D_{max} (Å)	139 ± 5	87 ± 5
Porod volume estimate ($Å^3$)	144130 ± 4200	73567 ± 5000
Dry volume calculated from sequence ($Å^3$)	53494	33262
*Molecular mass determination**		
Contrast ($\Delta\rho$ x 10^{10} cm^{-2})	3.047	3.047
Molecular mass M_r (from $I(0)$)	66366 ± 5000	24870 ± 2000
Molecular mass M_r (from Porod volume)	90081 ± 24000	45979 ± 5000
Calculated monomeric M_r from sequence	44210	27491
Software employed		
Primary data reduction	Automated radial averaging (65)	
Data processing	*PRIMUS*	
Ab initio analysis	*DAMMIF, MONSA*	
Validation and averaging	*DAMAVER*	
Rigid body modelling	*CORAL, EOM*	
Computation of model intensities	*CRYSOL*	
3D graphics representations	*PYMOL*	

patterns from available high resolution models were calculated using the program CRYSOL (50) and used to determine the fit of these models to the experimental data. Given the atomic coordinates, the program minimizes discrepancy in the fit to the experimental scattering intensity by adjusting the excluded volume of the particle and the contrast of the hydration layer. The discrepancy (χ^2) between the measured and calculated SAXS profiles is defined as follows.

$$\chi^2 = \frac{1}{N-1}\sum_j \left[\frac{I_{exp}(s_j) - cI_{calc}(s_j)}{\sigma(s_j)}\right]^2 \qquad \text{(Eq. 1)}$$

where N is the number of experimental points; c is a scaling factor; $I_{calc}(s_j)$ and $I_{exp}(s_j)$ are the calculated and experimental scattering intensity, respectively; and $\sigma(s_j)$ is the experimental error at the momentum transfer s_j. The statistics of data collection are summarized in Tables 3 and 4.

SAXS Modeling

Ab initio models were reconstructed from the ETR1-ΔTM scattering data using the simulated annealing bead modeling programs DAMMIF (51) and MONSA (52). DAMMIF and MONSA represent the particle as a collection of M ($\gg$1) densely packed beads inside a loosely constrained search volume compatible with the experimentally determined R_g (DAMMIF) or D_{max} (MONSA). In the case of MONSA, three bead phases were defined corresponding to the GAF, DHp and CA, and RD domains, and data from three ETR1 constructs ($ETR1^{DHp-CA}$, $ETR1^{DHp-CA-RD}$, and the entire ETR1-ΔTM) were used in a global refinement procedure. An average of 10 independent reconstructions was used to generate a representative shape envelope using the program DAMAVER (53). In addition, the ensemble of the DAMMIF *ab initio* models was used to calculate an excluded volume of the particle, V_{DAM}, from which another independent MM estimate was derived (empirically, $MM_{DAM} \sim V_{DAM}/2$).

Rigid body models were generated for all constructs using the program CORAL (54) where high resolution models of domains were defined as rigid bodies, and linkers/loops between the individual subunits were represented as flexible random polypeptide chains. The results of 10 independent CORAL runs were analyzed using the programs SUPCOMB13 (55) and DAMAVER to identify the most representative/typical models.

Three homology models of the cytoplasmic domains of ETR1 were constructed in the program MODELLER (v9.10) (56) based on the DHp domain of ERS1, the structures of the CA and receiver domains of ETR1 (Protein Data Bank code 1DCF (31)), and three homologous GAF domains (Protein Data Bank codes 2O9B (30), 2LB5 (57), and 1MC0 (58)). The DHp and the GAF domains were mutated to match the residues in ETR1. The *T. maritima* TM0853 HK domain (Protein Data Bank code 2C2A) was used to place the DHp and CA domains relative to each other. The GAF domains were placed using the overlap with the N terminus of the DHp^{ERS1} domain as a guide. The receiver domain was placed relative to this core model by rigid body modeling with a 15-residue flexible linker between the CA and receiver domain as a restraint.

Flexibility analysis of ETR1 in solution was conducted using the constructed rigid body models as input for the ensemble optimization method. This approach seeks to best fit the experimental scattering profile with an ensemble of conformations (59). The 15-residue linker between the CA and receiver domains was defined as flexible, and its possible conformations were modeled with RANCH producing 10,000 random configurations (59), whereas the rest of the dimeric protein was kept fixed. A genetic algorithm was used to find the set of conformations best fitting the SAXS data. The structures selected from the random pool of structures were analyzed with respect to the R_g distribution.

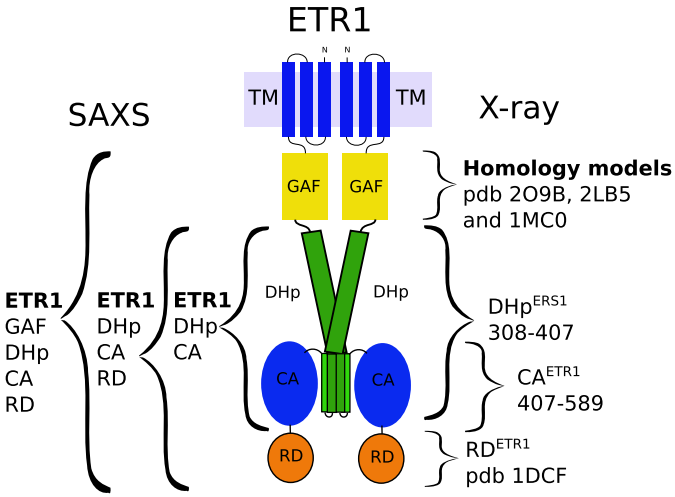

FIGURE 1. **Schematic model of an ETR1 dimer with *curly brackets* indicating the borders of the constructs used to assemble the final model.** Constructs used for SAXS measurements are on the *left*, and the homology models and crystal structures are on the *right*. The crystal structures of the ERS1 DHp domain and the ETR1 CA domain and all the SAXS models are described in this work. *TM*, transmembrane domain.

RESULTS

An overview of the domain denominations and of the various constructs used for the modeling, including their termini and structural analysis method, is given in Fig. 1.

Structure of the DHp Domain of ERS1—Attempts to crystallize the ETR1 DHp domain did not yield suitable crystals, whereas DHp^{ERS1} crystallized in two different space groups under similar crystallization conditions. Crystals in space group (SG) $C222_1$ contained one dimer per asymmetric unit and diffracted x-ray radiation to 1.9 Å, whereas crystals in SG $P2_12_12$ contained two dimers per asymmetric unit and diffracted x-rays to 2.15-Å resolution. Attempts to solve the structure by molecular replacement failed probably due to the parallel packing of the long helical segments in both crystal forms. Phasing of the data succeeded through SAD of protein labeled with Se-Met.

As expected from previously described prokaryotic homologues (14), the eukaryotic DHp^{ERS1} forms a dimer of helical hairpins (Fig. 2*A*). The two antiparallel helices of a hairpin are connected by a short loop (res. 371–375). The N-terminal helix α1 (res. 308–370) extends for about 95 Å and is considerably longer than in all known prokaryotic structures. The length of the C-terminal helix α2 adds up to about 40 Å and closely resembles helix α2 of the complete HK from *T. maritima*, HK853 (Protein Data Bank code 2C2A). The first ~30 residues of helices α1 and α1′ (the prime discerns the protomers within a DHp dimer) form a parallel coiled coil with a left-handed twist of about 23°. The remaining parts of the hairpins constitute a four-helix bundle. Therefore, DHp^{ERS1} consists of two parts, a coiled coil portion and a four-helix bundle, comparable with the dimerization domain of HK853. Because helix α1 of DHp^{ERS1} is about five turns longer than in HK853, the coiled coil domain is correspondingly longer as well. The entire dimer interface buries 2120 $Å^2$ of solvent-accessible surface area from each monomer. The four-helix bundle contributes 1310 $Å^2$ or 62% of this interface. The coiled coil interface contributes 810 $Å^2$, which is about 40% more than in HK853.

Because the structure of HK853 contains a crystallographic dyad, both hairpins are by definition identical. The situation for DHp^{ERS1} with three crystallographically independent copies of dimerization domains is different and reveals a number of intradimer discrepancies. Each N-terminal helix displays a noticeable kink at residue Met-351 just 2 residues prior to the phosphoryl-accepting His-353. Both bending angles within each dimer are significantly different but strikingly comparable among individual dimers. When superimposing all three independent copies of DHp^{ERS1} from the conserved histidine residue to their C termini (residues 353–404), the bending is always about 18° in helix α1 and always about 31° in helix α1′ (Fig. 2*B*). The conserved phosphorylatable His-353 adjacent to the kink region is solvent-exposed and assumes a variety of side chain orientations.

The larger bending of α1′ coincides with a hydrogen bond between the side chain amide of Asn-352′ located at the inner bend of the kink and the backbone carbonyl of Ile-396 in helix α2 that disrupts the canonical helical hydrogen bonding pattern of helix α1′. In SG $C222_1$, the side chain amide of Asn-352′ and the backbone carbonyl of Ile-396 are within 2.9 Å (Fig. 2*C*). This close contact correlates with an increase of the distance between the backbone carbonyl oxygen of Val-350′ and the backbone amide of Glu-354′ to 5.2 Å. The corresponding gap represents the outer angle of the helical kink. When there is no interaction between Asn-352 and Ile-396 ($d = 4.5$ Å) as in helix α1, the helical hydrogen pattern is preserved with a regular distance of 2.8 Å. The same pattern is found in all three independent dimers of DHp^{ERS1}.

The most conspicuous and functionally significant difference between the dimerization domains of HK853 and DHp^{ERS1} concerns the topology of the hairpin loops connecting helices α1 and α2. They are orthogonal to each other, resulting in an opposite handedness of the four-helix bundles (Fig. 2*D*). As a consequence, we expect ERS1 to perform a classical trans-phosphorylation because HK853 had been shown to phosphorylate in *cis* (14).

Any comparison of the dimerization domains of DHp^{ERS1} and HK853 must take their opposite handedness into consideration. Superposition of spatially equivalent helical residues therefore matches one hairpin of DHp^{ERS1} with helix α1 (res. 234–277) and helix α2′ (res. 286′-313′) from HK853. An r.m.s.d. of 1.1 Å between the less bent hairpin of DHp^{ERS1} and HK853 stresses the overall similarity of the dimerization domains despite their different connectivity. A higher r.m.s.d. of 1.6 Å between the stronger bent hairpin of DHp^{ERS1} and HK853 reflects the structural rearrangement of helix α1′ in DHp^{ERS1}. For comparison, the intramolecular r.m.s.d. between the hairpins of the dimer of DHp^{ERS1} in SG $C222_1$ is 1.8 Å.

Structure of the Catalytic Domain of ETR1—CA^{ETR1} crystallized in space group $I2_12_12_1$ with one molecule per asymmetric unit and diffracted x-rays to 1.90-Å resolution. The final model contains 150 protein residues, one ADP molecule, 11 Cd^{2+} ions, one Cl^- ion, and one acetate (Fig. 3*A*). The overall structure assumes an α/β-sandwich fold and closely resembles the CA domain of HK853. Following the nomenclature of HK853,

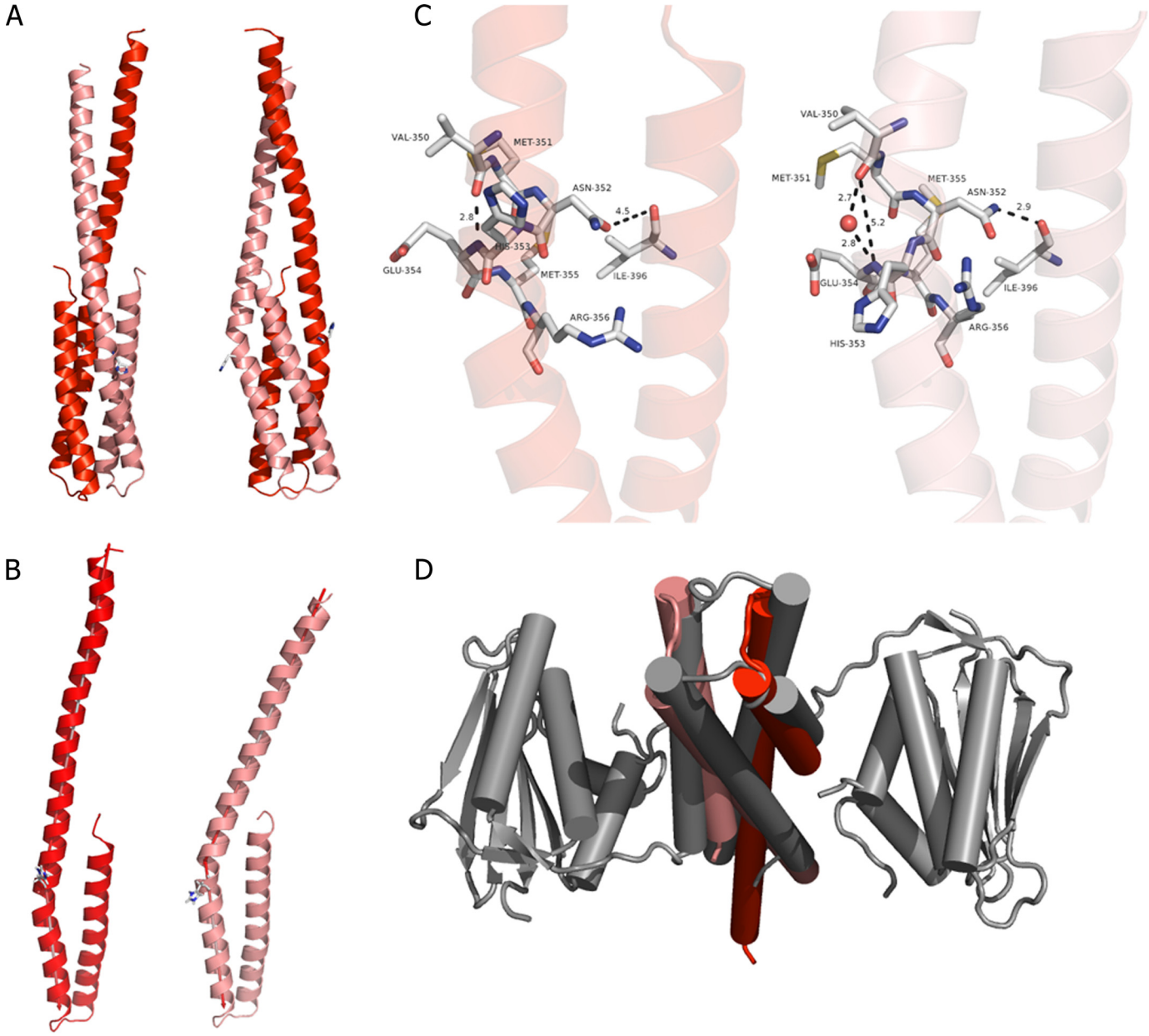

FIGURE 2. **Dimerization domain of ERS1 (DHp^{ERS1}).** *A*, schematic representation in two orientations separated by 90°. The two hairpins per dimer are colored *dark* (chain A) and *light red* (chain B), respectively, with the scheme being preserved in all panels of the image. *B*, superposition of DHp^{ERS1} (res. 353–404) highlighting the effect of the kink on the N-terminal section of the domain. The axis used to calculate the angle between the helices is indicated. *C*, comparison of the region around the phosphoryl-accepting histidine residue (shown as *sticks*) with α1 (small kink; *left*) and α1′ (large kink; *right*) with selected residues shown as *sticks* and atom distances shown as *dashed lines*. *D*, comparison of the topology of the hairpin loops of DHp^{ERS1} (*red*) and HK853 (*gray*).

one layer of the sandwich fold consists of a mixed five-stranded β-sheet (βB and βD–βG), and the other layer consists of three helices (α3–α5) and a pair of short antiparallel β-strands (βA and βC). Two loops, residues 490–502 and residues 531–543, could not be modeled due to weak electron density. The first loop connects strands βD and βE and exceeds the equivalent loop in HK853 by 16 residues. The second loop constitutes the ATP lid, which is also partially unstructured in HK853. 138 equivalent pairs of Cα atoms from CA^{ETR1} and HK853 overlay with an r.m.s.d. of 1.4 Å.

The Nucleotide Binding Site—An ADP molecule is bound at the expected nucleotide binding site of CA^{ETR1} in a conformation that emulates the ADP bound by HK853. It interacts with conserved residues from the N, G1, F, G2, and G3 boxes. The purine ring of the ADP is tucked into a hydrophobic pocket formed by Phe-474, Ile-518, and Ile-526. The interaction of Phe-474 with both the purine and Lys-473 classifies the HK of ETR1 as belonging to the predominant class of histidine kinases like PhoQ and HK853 (60). The adenine is further fixed by a hydrogen bond between the conserved Asp-513 of the G1 box and N6 of the exocyclic amino group. The only interaction of the ribose is a hydrogen bond between O2′ and the Nϵ of Lys-529 in the F box. This interaction is unusual; however, the side chain of Lys-529 has B-factors of more than 80 Å^2 and accordingly weak electron density. In CA^{ETR1} and HK853, the last structured residues before the unstructured ATP lid point in

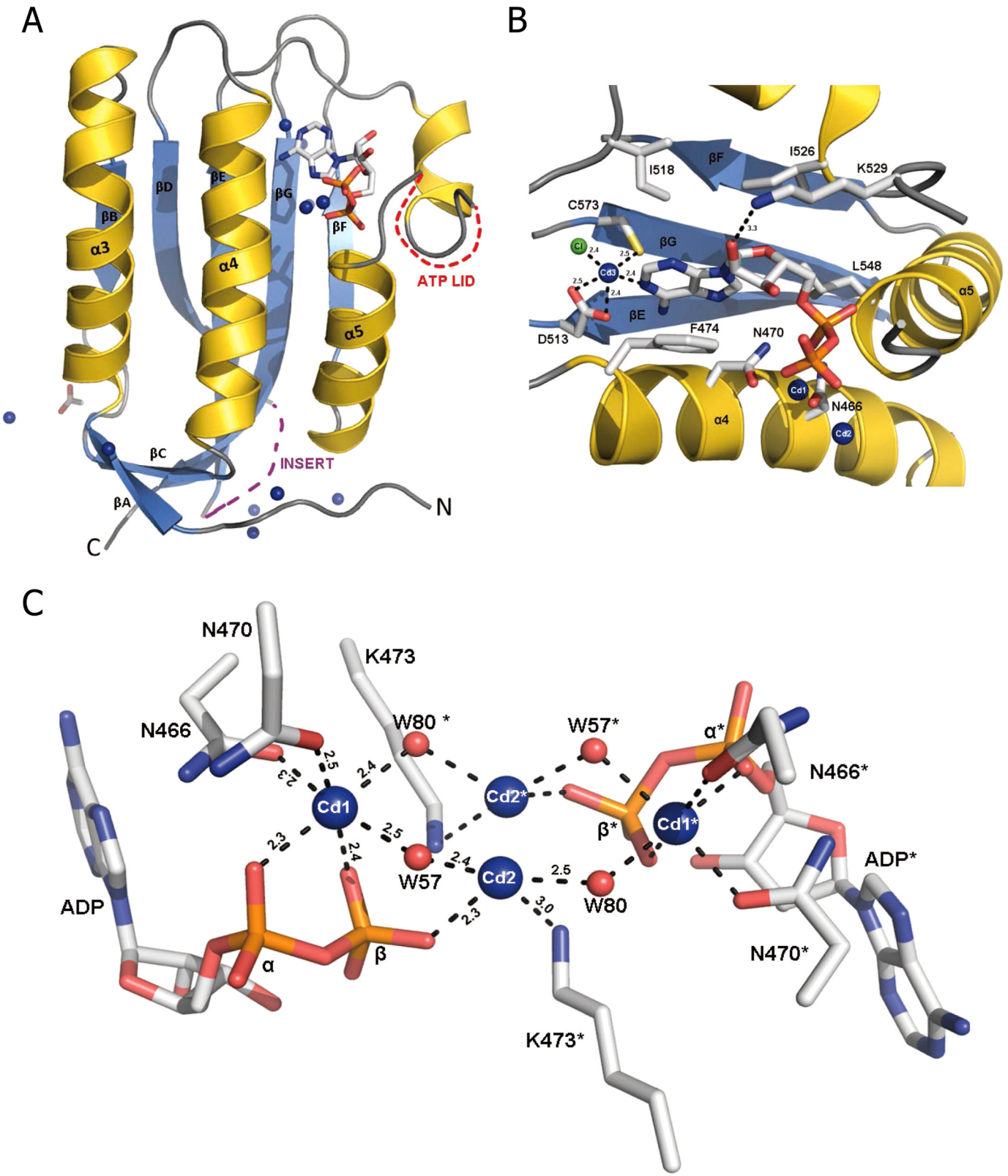

FIGURE 3. **Catalytic domain of ETR1 (CA^{ETR1}).** *A*, schematic representation of CA^{ETR1} in complex with ADP. The plant-specific insert residues (490–502) and the ATP lid (531–435) are disordered and shown as *dashed lines*, the ADP and acetate are shown as *sticks*, and the metal ions are shown as *spheres*. *B*, the CA^{ETR1} nucleotide binding side with ADP and interacting residues shown as *sticks*. A hydrophobic pocket formed by residues Phe-474, Ile-518, and Ile-526 covers the adenine moiety of ADP. A cadmium ion is coordinated among N1 of adenine ring, the residues Asp-513 and Cys-573, and a chloride ion (*green sphere*). Binding of this metal ion requires the G3 box motif residue Cys-573, which is present only in the ethylene subfamily 1 receptors. *C*, Cd^{2+} coordination with phosphate groups of ADP. Ions are shown as *spheres*, and interacting residues are shown as *sticks*. Two cadmium ions (*blue spheres*) interacting with water molecules (*red spheres*) and the phosphate groups of ADP and the interacting residues (*sticks*) are shown. The α- and β-phosphate oxygen atoms of the ADP, Asn-470, Asn-466, and two water molecules (*W57* and *W80*) octahedrally coordinate the ion. Symmetry-related ions and residues are highlighted with an *asterisk*.

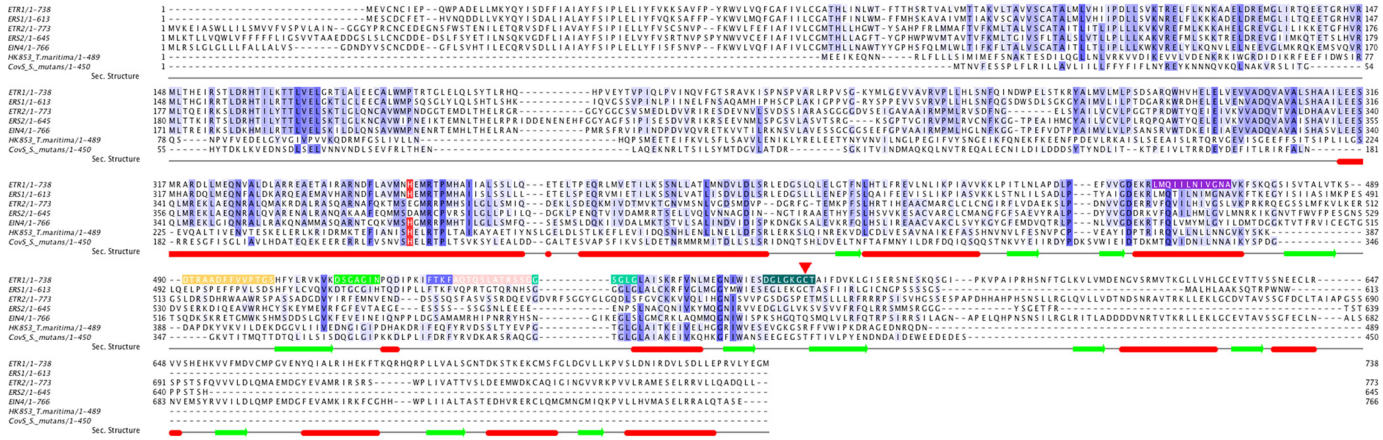

FIGURE 4. **Annotated alignment of ethylene receptors and two bacterial histidine kinases.** *Red tubes* and *green arrows* annotate the secondary (*Sec.*) structure as observed in the structures. Conserved features are indicated with the phosphorylatable His in *red*, the N box in *purple*, the plant-specific insert in *orange*, the G1 box in *light green*, the F box in *blue*, the ATP lid in *salmon*, the G2 box in *green*, and the G3 box in *dark green*. The cysteine residue (Cys-573) from the G3 box motif is highlighted with an *arrow*. This cysteine residue is required for Cd^{2+} binding and is found only in subfamily 1 receptors (ETR1 and ERS1). In subfamily 2 receptors (ETR2, ERS2, and EIN4), this cysteine is replaced by larger residues, which are not suitable to accommodate the binding of a cadmium ion.

opposite directions. Although the loop wraps around and over the ADP in HK853, it departs from the nucleotide in CA^{ETR1}. This departure points the loop toward the inferred regulatory interface with the DHp domain based on analogy with HK853. As in HK853, the O3′ of the ribose is in hydrogen bonding distance of its own β-phosphate. The α- and β-phosphates are positioned similarly as in HK853 by interactions with Asn-470, the main chain amide of Leu-548, and the already mentioned Lys-473 (Fig. 3*B*). The disorder of the ATP lid (res. 531–543 in CA^{ETR1} and res. 433–441 in HK853) was blamed on the absence of a γ-phosphate in HK853 (60, 61). The shorter ATP lid of the CA domain of ThkA (Protein Data Bank 3A0T), however, is flexible in the ligand-free form but ordered in the ADP-bound form (62). The conformation of the ATP lid, therefore, appears to depend on multiple parameters.

Positions of the Metal Binding Sites—CA^{ETR1} was crystallized in the presence of $CdSO_4$. Crystallization attempts in the absence of nucleotide or $CdSO_4$ were as unsuccessful as attempts to replace Cd^{2+} with Mg^{2+} or Mn^{2+}. Based on SAD data, a total of 11 Cd^{2+} sites per monomer were identified. Eight of these sites are located on the protein surface in close contact with appropriate side chains. The remaining three sites mediate interactions between protein and ADP.

Two cadmium ions are ligated by the phosphate groups. Oxygens of the α- and β-phosphates, the side chains of Asn-466 and Asn-470, and two water molecules octahedrally coordinate one ion (Fig. 3*C*). The position of this Cd^{2+} ion is equivalent to the position of the Mg^{2+} ion in the AMPPNP complex of PhoQ (Protein Data Bank 1ID0). The second Cd^{2+} is very close to the crystallographic dyad parallel to the *c* axis. Accordingly, this cation interacts with the β-phosphates from symmetry-related ADP molecules in the adjacent asymmetric unit that are just 6.5 Å apart. The occupancy of this Cd^{2+} site was set to 50%.

In many histidine kinases, a water molecule mediates a contact between the conserved Asp-513 (Asp-415 in Protein Data Bank code 1ID0, Asp-411 in HK583, and Asp-533 in Protein Data Bank code 3SL2) from the G1 box and N1 of the adenine ring. In CA^{ETR1}, a Cd^{2+} takes this position. Cys-573 and a Cl^- ion complete a tetrahedral ligand sphere around this Cd^{2+} (Fig. 3*B*). This cysteine residue is part of the G3 box motif and found only in subfamily 1 but not in subfamily 2 receptors (ETR2, ERS2, and EIN4) (Fig. 4). Here, the cysteine is replaced with glutamate, lysine, and glutamine, respectively, which are much larger in size and accordingly unsuitable to accommodate the binding of a cadmium ion.

SAXS Model of the Cytosolic ETR1 Receptor Domain—A construct of ETR1 comprising the entire cytosolic domain (ETR1-ΔTM; res. 158–738) was analyzed by SAXS after resisting vigorous crystallization attempts. ETR1-ΔTM tends to aggregate, which prevented acquisition of usable data at high sample concentrations (>1 mg/ml). The sensitivity of the sample also prevented the acquisition of useful SAXS data in the presence of nucleotides. The addition of the stabilizing agent NDSB (250 mM) to the sample facilitated measurement across an increased range of concentrations. The good data quality allowed a detailed structural modeling, especially at low angles, describing the overall shape of the particle.

Because of some uncertainty in the accuracy of protein concentration estimations for the ETR1 constructs, the MM was derived from hydrated particle volumes determined from the SAXS data and independent of sample concentration (Table 2). MM based on the Porod volume V_p is 160 ± 25 kDa, which is consistent with that expected for a dimeric receptor (130 kDa). Furthermore, the molecular envelope reconstructed from *ab initio* bead modeling can only be adequately fit by docking the high resolution domain fragments as a dimer into the model volume. Subsequent rigid body refinement of the crystallographic fragments as a dimer yields acceptable goodness-of-fit parameters with discrepancies (χ) between the experimental data and rigid body models in the range $1.1 < \chi < 1.5$, further providing strong evidence that ETR1-ΔTM is dimeric in solution (Fig. 5*A*).

SAXS data for the entire soluble domain of ETR1 and two shorter constructs ($ETR1^{DHp\text{-}CA}$ and $ETR1^{DHp\text{-}CA\text{-}RD}$) were used in global refinement procedures to determine the low resolution solution structure of ETR1-ΔTM (Fig. 4*A*). Multiphase bead models defining three distinct phases were reconstructed *ab initio* from the three data sets: 1) GAF domain, 2) DHp and

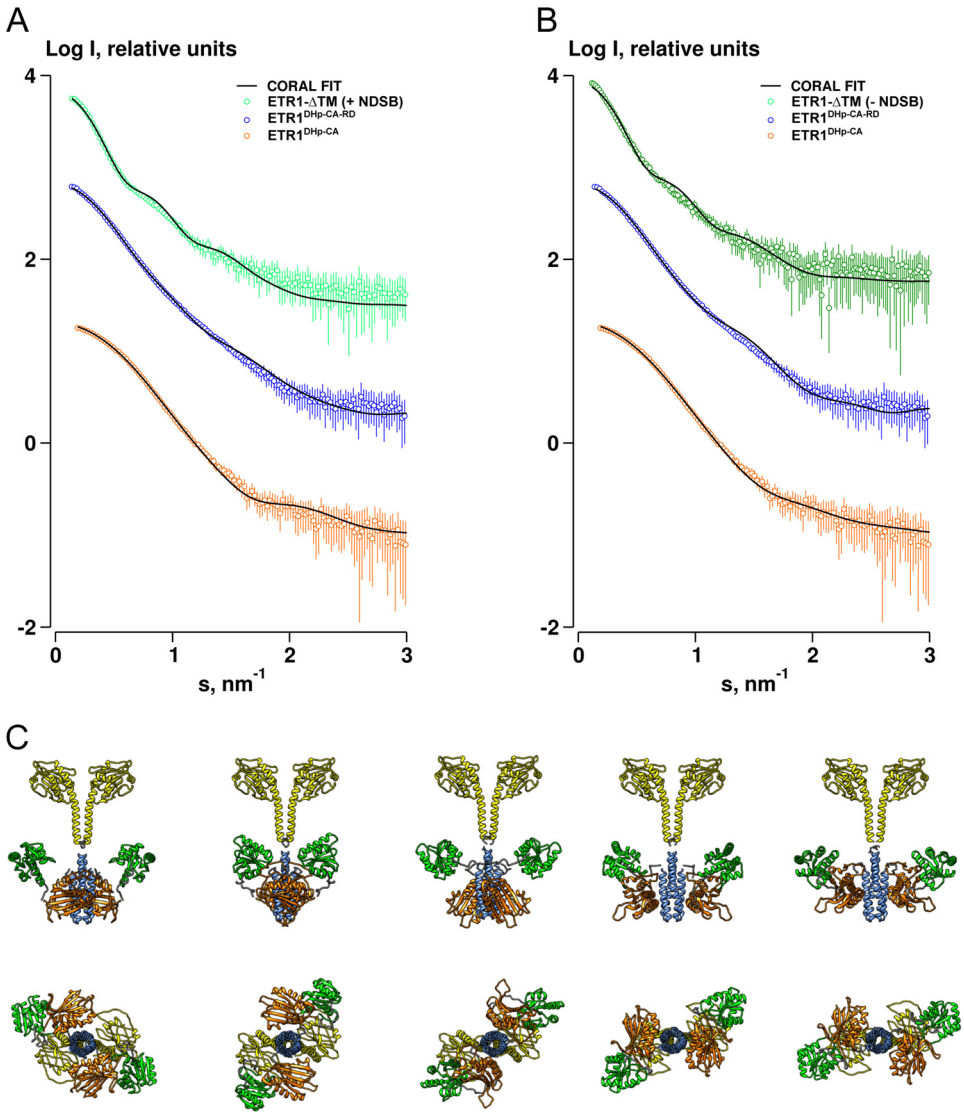

FIGURE 5. **Rigid body refinement of ETR1-ΔTM.** *A*, model refined in a global fit against data from three constructs, including 250 mM NDSB data for the cytoplasmic domains of ETR1. Discrepancies (χ) for the fit of the models to the ETR1-ΔTM, ETR1$^{DHp\text{-}CA\text{-}RD}$, and ETR1$^{DHp\text{-}CA}$ data with 250 mM NDSB are 1.5, 1.1, and 1.3, respectively. Discrepancies (χ) for the fit of the models to the ETR1-ΔTM, ETR1$^{DHp\text{-}CA\text{-}RD}$, and ETR1$^{DHp\text{-}CA}$ data without NDSB are 1.4, 1.2, and 1.4, respectively. *B*, model refined as in *A* but using data without NDSB for the cytoplasmic domains of ETR1 at low protein concentration. *C*, ensemble of rigid body models of ETR1-ΔTM refined against SAXS data. Models at the *bottom* are rotated through 90° relative to those above. The GAF, DHp, CA, and RD domains are colored *yellow*, *blue*, *orange*, and *green*, respectively.

CA domains, and 3) RD domain. A global refinement was conducted, generating dimeric models with a "dumbbell" shape for both ±NDSB data and with the GAF and RD domains at opposing sides of the central DHp dimer interface and CA domains (Fig. 4*D*). Independent of the *ab initio* modeling, the available high resolution data of the ETR1 domains were also used in a multicurve global rigid body refinement procedure (Fig. 5, *A* and *B*). Structural information of the GAF domain was derived from homology modeling because all attempts to obtain crystallographic information of the GAF domain of ETR1 failed. Three GAF domains with different functional backgrounds gave virtually identical results in rigid body refinements against SAXS data (Fig. 4*C*). The features of the dimeric ETR1-ΔTM models are shown in Fig. 5*C* where the CA domains and RD domains extend outward from the central DHp helical stalk. There appears to be little contact under the conditions used in the measurement between the catalytic and receiver components themselves or between the RD domain and the dimerization domain. The CA domain, however, appears consistently associated with the DHp domain in a similar manner as (but distinct from) that observed in the *T. maritima* crystal structures (Protein Data Bank codes 3DGE and 2C2A). When the best rigid body model is superimposed with the multiphase bead model (Fig. 4*D*), the agreement in terms of overall shape is excellent. However, the bead model suggests that the average position of the CA domain is distinct from that observed in the rigid body model where it is closer to the GAF domain. Also, in the fits of the rigid body model to the data for the complete cytosolic region both with and without NDSB, the maxima at $\sim s = 1$ nm^{-1} is somewhat smeared out. Taken together, this may reflect a dynamic and flexible nature of the linkers between the peripheral domains.

To further explore the potential flexibility of the cytosolic domain of ETR1, an ensemble-based modeling approach was

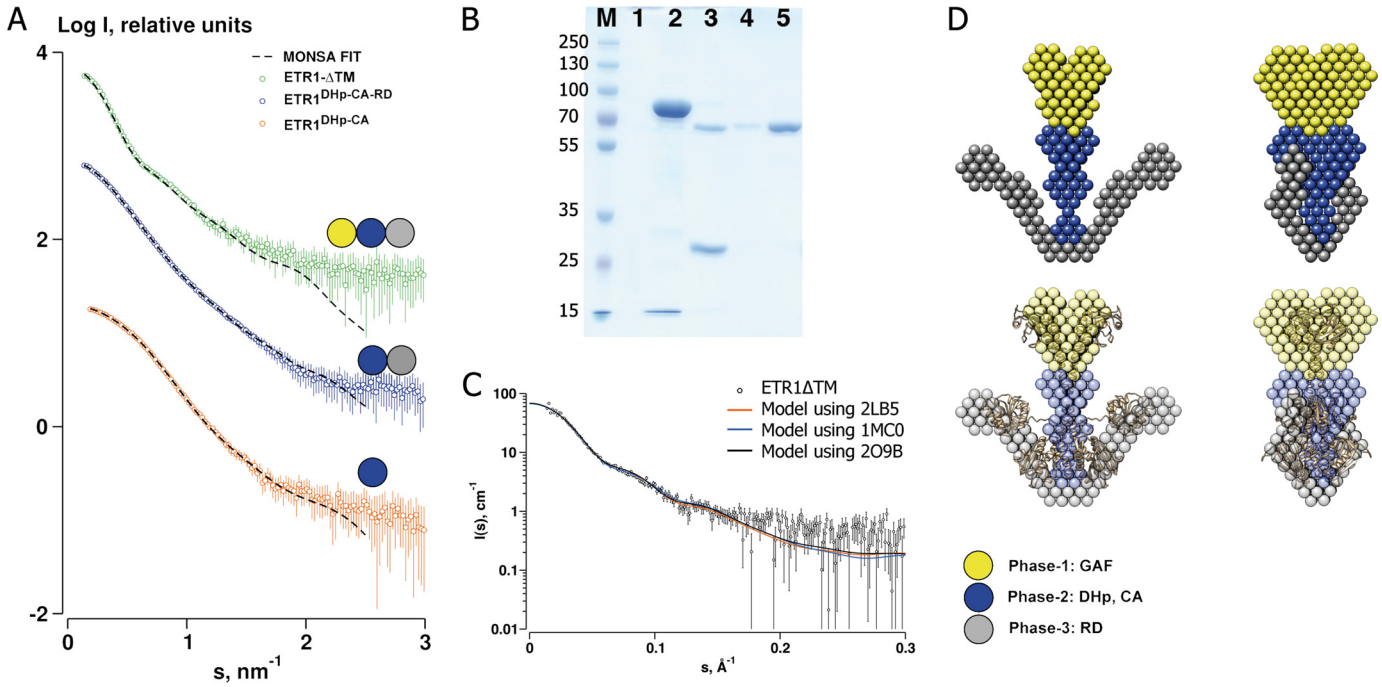

FIGURE 6. **Multiphase *ab initio* reconstruction of ETR1-ΔTM.** *A*, global fits of the models reconstructed from data for three constructs of ETR1 (ETR1-ΔTM, $ETR1^{DHp\text{-}CA\text{-}RD}$, and $ETR1^{DHp\text{-}CA}$) with the model bead phases corresponding to each data set indicated. *B*, SDS gel of ETR1-ΔTM during different steps of the purification. *Lane M*, marker; *lane 1*, empty; *lane 2*, pooled fractions after the Ni-NTA step; *lane 3*, after the tobacco etch virus step; *lane 4*, after the second Ni-NTA step; *lane 5*, concentrated protein used for SAXS. *C*, rigid body refinement of ETR1-ΔTM with three homologous but dissimilar GAF domains against data of ETR1-ΔTM. *D*, the reconstructed multiphase models overlaid with the best rigid body model (*bottom*). Models on the *right* are rotated 90° about the vertical axis.

conducted using the ensemble optimization method (59). An ensemble of models was selected from a pool of randomly generated conformations that best describe the experimental data. Models were constructed from the high resolution domain structures with randomized DHp-CA and CA-RD linkers, maintaining the fixed position and orientation of the GAF and DHp domains. The selected ensembles provide an improved description of the data, accounting for the smearing out of the maxima at $s \sim 1.0$ nm^{-1} by modeling domain flexibility (Fig. 6*B*). The size distributions generated in this procedure suggest that the system is not completely flexible as the widths of the selected ensembles relative to the pool are visibly more narrow (Fig. 6*A*). It is interesting to note that the distribution of R_g values for the data set in the absence of NDSB is shifted to higher values, an indicator of predominantly extended structures, whereas the NDSB data yield a distribution close to the average R_g of the pool. This suggests that the addition of a stabilizing agent to the solution promotes the formation of more compact structures.

Agreement between independent modeling approaches confirmed the expected dimeric assembly of ETR1. The overall dumbbell shape obtained by *ab initio* modeling correlates well with the rigid body model, positioning the GAF domain at the top and the catalytic and receiver domains at the bottom of a central helical bundle, respectively. There seems to be some flexibility of the receiver domain position, but it appears to be distinct from the position described for a *T. maritima* receiver domain in complex with its HK (14).

DISCUSSION

Signal transduction involves the activation of cytosolic proteins by membrane-bound receptors. Specific protein-protein interactions between the receptor and its intracellular target molecules constitute the foundation of this process, which is modulated by structural rearrangements in the cytosolic domain of the receptor. Any detailed understanding of signal transduction, therefore, requires structural knowledge of the different conformational states of the receptor and its complexes. Our results provide the first model of the entire cytosolic domain of the main ethylene receptor, ETR1, together with indications of specific conformational rearrangements of its central cytosolic domain.

The Dimerization Domain—A distinct feature of the isolated DHp domain of ERS1 is its inherent asymmetry. In three independent copies of DHp^{ERS1}, the bending angles of the N-terminal helices at Met-351 consistently amount to about 18° for helix α1 and 31° for α1′, the second helix of the dimer. In all three cases, the larger bending angle (helix α1′) correlates with a hydrogen bond between the side chain amide of Asn-352′ located at the inner bend of the kink and the backbone carbonyl of Ile-396 in helix α2 and with a disruption of the direct helical hydrogen bond between Val-350′ and Glu-354′ by a water molecule. Asn-352 is conserved in subfamily 1 and substituted with a serine, another potential hydrogen donor, in subfamily 2 (Fig. 9). The canonical hydrogen bond of the dimer-related helix is extended but maintained over the 18° kink. Molecular dynamics calculations on DHp^{ERS1} indicate that the observed asymmetry is dynamic in nature such that the less bent helix may assume the higher bent state at the expense of the other helix, which simultaneously transitions from a high to a less bent state (data not shown).

The sections of individual hairpins before (res. 312–340) and after (res. 356–405) the kink overlay well with r.m.s.d. values of

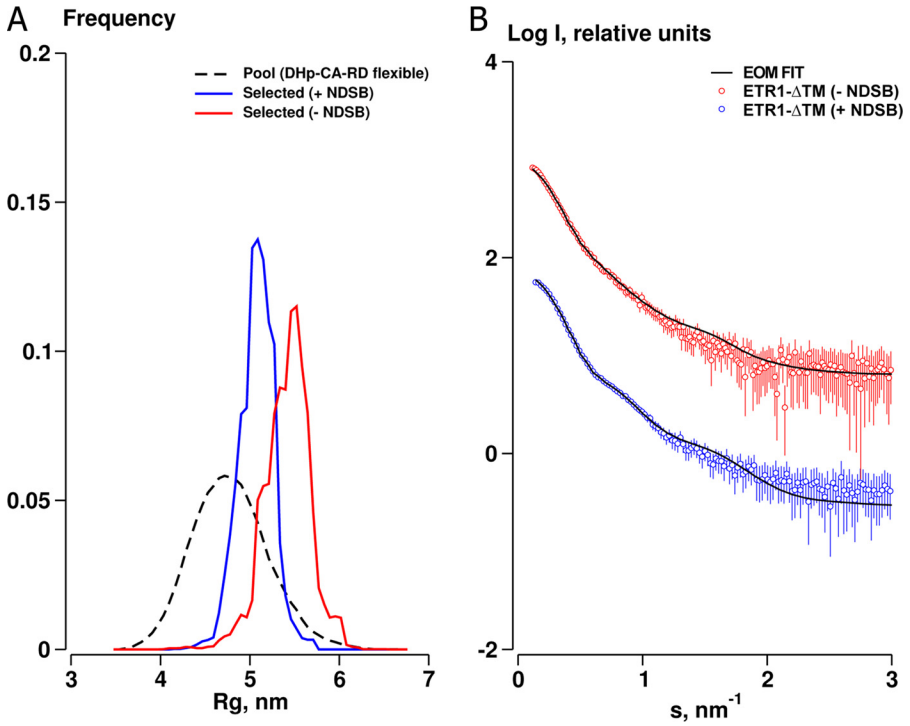

FIGURE 7. **Domain flexibility analysis of ETR1-ΔTM.** *A*, R_g distributions from the ensemble optimization method analysis using ±250 mM NDSB. Runs were conducted with both DHp-CA and CA-RD linkers defined as flexible. *B*, fits of the selected ensemble optimization method (*EOM*) ensemble to the experimental data. Discrepancies (χ) for the fit of the models to the ETR1-ΔTM data with and without 250 mM NDSB are 1.2 and 1.1, respectively.

about 0.75 Å for the prekink sections and about 0.45 Å for the postkink sections. The region around the kink between residues 341 and 355 overlays with an r.m.s.d. value of about 1.4 Å. In contrast to the pre- and postkink sections, this part at the intersection of the coiled coil and four-helix bundle does not follow the classical knobs-into-holes packing of buried side chains, which is reflected in variability of the Crick angle, radius, and angular shift (especially in chain A as analyzed using the program samCC (63)) (Fig. 7). The asymmetry is also found on the level of side chains participating in the interhelix contacts. Helices α1 and α2 of chain A show a cogwheel-like movement relative to each other when compared with chain B. This is most prominent at the end of chain A, the domain boundary to the catalytic CA domain, after residue 399; *e.g.* residue 402 in helix α2′ (chain B) points to the core of the four-helix bundle, whereas the same residue in helix α2 points to the solvent (Fig. 8). The observed asymmetries at both termini of the central dimerization domain are expected to influence the orientation of the preceding GAF domains and the succeeding catalytic domains.

Previously, different rotational states of a charged layer within two-component HKs were correlated with different activity states of the HK (17). In DHp^{ERS1}, this region corresponds to the residues around Arg-344 at the intersection of the coiled coil and four-helix bundle. Arg-344 of helix α1 points to the center of the bundle, whereas Arg-344 of helix α1′ points toward the surface with a Crick angle difference of about 20° between both. This asymmetric arrangement is neither in line with a knobs-into-holes nor an *x-da* arrangement (Fig. 8). A similar configuration is observed in variants of the DesK, another HK domain (16). Therefore, this arrangement flanked with regular arrangements before and after the kink likely constitutes the conformation of the DHp domain in the absence of external restraints. The observed conformations at least highlight a highly flexible hinge within DHp^{ERS1} close to the phosphoryl-accepting histidine. This hinge within the long helix α1 is capable to simultaneously bend and rotate. Because we observed no other conformational state of this domain in its isolated state, it likely represents the structural ground state of the DHp domain.

The connecting loops at the tip of the four-helix bundle of the five receptors in *A. thaliana* appear to fall into two sequentially related groups. Subfamily 1 sequences from *A. thaliana* as well as members from subfamily 1 from other plants are highly conserved, whereas the sequences of subfamily 2 are diverse. Therefore, the topology of subfamily 1 dimerization domains is expected to be left-handed, whereas no prediction of the connectivity can be made for subfamily 2. The connectivity of the hairpin domains in DHp^{ERS1} suggests a transphosphorylation mechanism as already observed for other HKs (64).

The interface of the N-terminal coiled coil of DHp^{ERS1} contains a number of polar or charged residues (Ser-316, Arg-320, Asn-327, and Arg-334) at the a or d positions of the helical heptad. Charged residues at position *a* or *d* were also found in the HKs EnvZ and Sln1, making this a general feature of coiled coils in HKs. The interface residues of the five ethylene receptors in *A. thaliana* at position *a* or *d* between residues 313 and 337 are conserved or conservatively replaced (*R* for *K* in two receptors). This strongly suggests coiled coils of similar length and crossing angles in all of them.

The Catalytic Domain—The structure of the catalytic domain in complex with ADP is highly similar to that of the

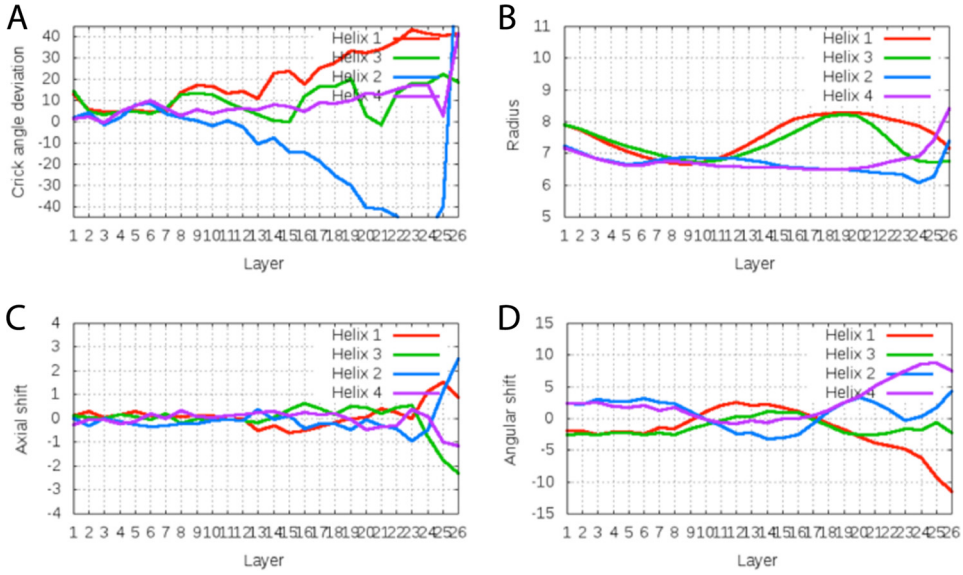

FIGURE 8. **Results of the analysis using the program samCC for DHP^{ERS1} in SG C222$_1$.** The numbering of the helices from *1* to *4* corresponds to helix α1, α2, α1′, and α2′, respectively. Values are given for each layer of the four-helix bundle.

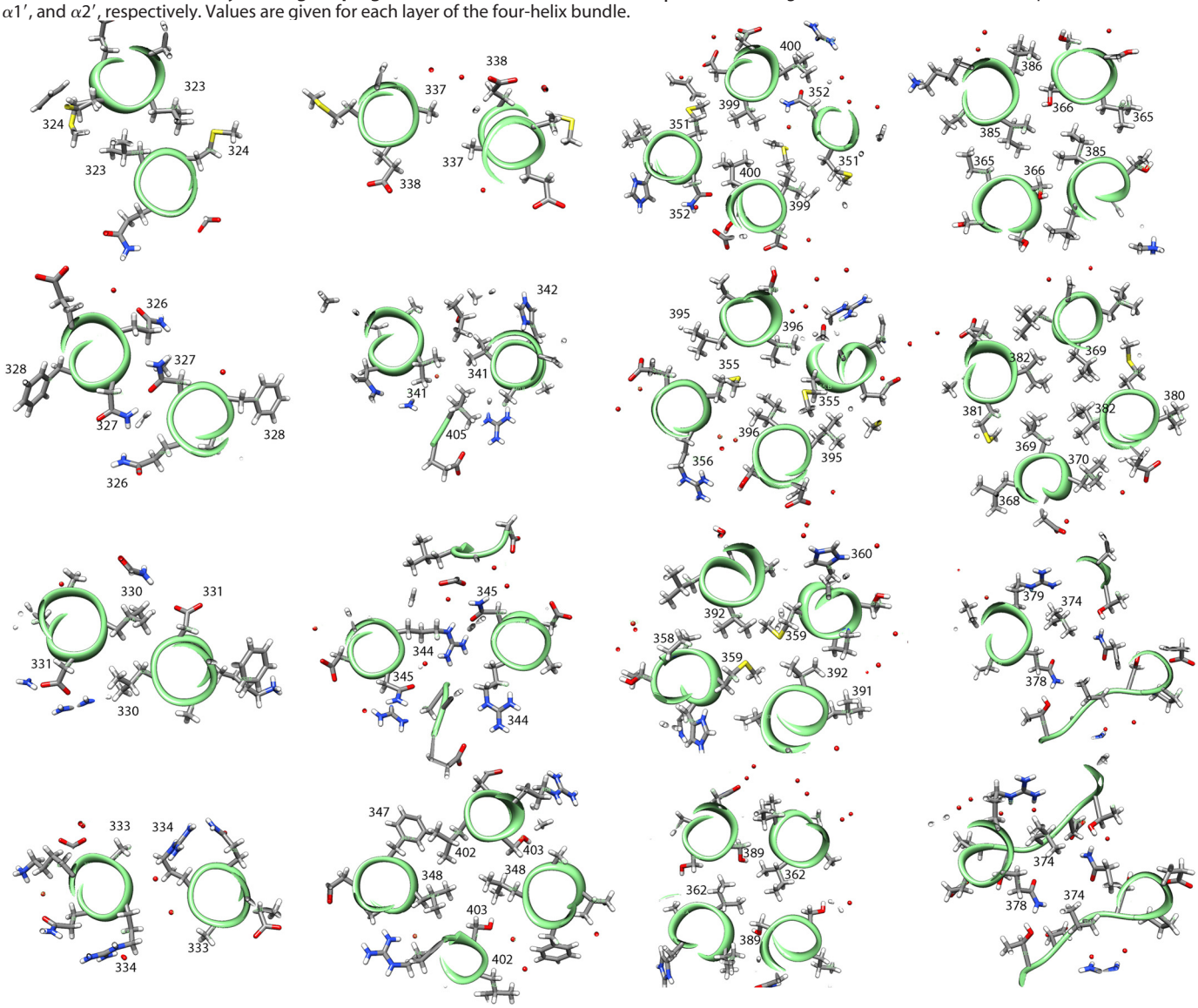

FIGURE 9. **Individual cross-sections of the DHP^{ERS1} structure.** The numbering corresponds to the amino acids in ERS1. The helices were approximately perpendicular to the view axis. Residues outside of the layer in focus were excluded for clarity. Residues are shown as *sticks*, and water is shown as *red spheres*.

catalytic domain of the complete prokaryotic HK853. The largest structural differences are located in a loop connecting the F box and G2 box motifs, which comes closest to the interface between the dimerization and catalytic domains. Another significant difference was found within the ADP binding pocket. Ordinarily, a water molecule mediates the interaction between the conserved aspartate of the G1 motif and the endocyclic N1 of the purine. In CA^{ETR1}, the same interaction is mediated by a Cd^{2+} ion, which is further ligated by Cys-573 and a nearby anion, which was interpreted as a Cl^- ion. The identity of this Cd^{2+} was unambiguously determined by anomalous scattering. Although it is debatable, whether Cd^{2+} is the biological cation, the ligand sphere and available space strongly argue for the presence of a cation at this position in ETR1. Sequence comparison within the ethylene receptor family suggests that this binding site is limited to subfamily 1 and probably absent in subfamily 2 members because of the substitution of Cys by much larger amino acids.

The Cytosolic Domain of ETR1—The cytosolic domain of ETR1 resembles the shape of a dumbbell with the N-terminal GAF domain immediately adjacent to the ethylene-binding membrane domain, separated from the ATP-binding catalytic and receiver domains by the long coiled coils of the dimerization domains. There is no evidence of physical interaction between the GAF and CA domains, which are separated by at least 35 Å. The conformational freedom of the GAF domains is restrained by the preceding small disulfide-linked ethylene-binding membrane domains. It appears reasonable, therefore, to endow the coiled coil region of the DHp with the task of communicating ethylene binding between its binding site and the catalytic domain. The rigid body refinement of an asymmetric model, reflecting the different helical kinks observed for the DHp domain, against the SAXS data yielded a marginally lower quality of fit ($\chi = 1.3$) than that of a symmetric model ($\chi = 1.2$) (data not shown).

Our attempts to obtain SAXS data in the presence of ATP failed due to dramatically decreased data quality. SAXS measurements of the ATP-binding HK domain (DHp-CA) of ETR1 in the presence and absence of ATP did not reveal conformational differences at this level of resolution (data not shown). This finding, however, cannot exclude conformational rearrangements of the full-length receptor as a function of nucleotide binding.

The chimeric nature of our model (DHp from ERS1 and GAF from homologous sources) adds some incertitude. Because the DHp domains of ERS1 and ETR1 share 93% similarity (84% identity), anything but a very high degree of structural analogy between both proteins would be surprising. The fact that the quality of our SAXS model was virtually independent of the chosen GAF domain (Fig. 6*C*) shows that (i) no conclusion can be drawn as to the functional nature of GAF in our model and (ii) our model is a good representation of the solution structure of the cytosolic domain of ETR1.

In the SAXS model of the cytosolic domain of ETR1, the GAF and HK consisting of DHp and CA assume comparatively defined positions relative to each other. The receiver domains in contrast are flexible and do not assume a fixed position. A closer analysis of the range of conformations consistent with the experimental data reveals that the average center of mass distance between DHp and the receiver domain varies between 30 and 78 Å. In none of the models do the two receiver domains come close enough to form the specific interaction previously observed for the isolated domains (31) (Fig. 5*C*). However, in the most frequent conformation of the receptor dimer selected by an ensemble analysis, the receiver domains adopt an arrangement perfectly suited to mediate those specific interactions between receptor dimers. This interaction may contribute to the observed formation of inter-receptor complexes possibly in a phosphorylation-dependent manner. The RD domain would hence serve as a module controlling the known receptor interaction, which is responsible for the wide range of ethylene sensitivity rather than for phosphoryl relay.

Acknowledgments—We gratefully acknowledge the European Synchrotron Radiation Facility for provision of beam time at beamlines ID23-1 and ID29; Swiss Light Source for provision of beam time at beamline X06DA; and EMBL/DESY for access to the beamlines X12, X33, and P12 and Manfred Weiss for support.

REFERENCES

1. Stepanova, A. N., and Alonso, J. M. (2009) Ethylene signaling and response: where different regulatory modules meet. *Curr. Opin. Plant Biol.* **12,** 548–555
2. Schaller, G. E., Ladd, A. N., Lanahan, M. B., Spanbauer, J. M., and Bleecker, A. B. (1995) The ethylene response mediator ETR1 from *Arabidopsis* forms a disulfide-linked dimer. *J. Biol. Chem.* **270,** 12526–12530
3. Rodríguez, F. I., Esch, J. J., Hall, A. E., Binder, B. M., Schaller, G. E., and Bleecker, A. B. (1999) A copper cofactor for the ethylene receptor ETR1 from *Arabidopsis*. *Science* **283,** 996–998
4. Schaller, G. E., and Bleecker, A. B. (1995) Ethylene-binding sites generated in yeast expressing the *Arabidopsis* ETR1 gene. *Science* **270,** 1809–1811
5. Chen, Y.-F., Randlett, M. D., Findell, J. L., and Schaller, G. E. (2002) Localization of the ethylene receptor ETR1 to the endoplasmic reticulum of *Arabidopsis*. *J. Biol. Chem.* **277,** 19861–19866
6. Chen, Y.-F., Gao, Z., Kerris, R. J., 3rd, Wang, W., Binder, B. M., and Schaller, G. E. (2010) Ethylene receptors function as components of high-molecular-mass protein complexes in *Arabidopsis*. *PLoS One* **5,** e8640
7. Parkinson, J. S., and Kofoid, E. C. (1992) Communication modules in bacterial signaling proteins. *Annu. Rev. Genet.* **26,** 71–112
8. Chang, C., Kwok, S. F., Bleecker, A. B., and Meyerowitz, E. M. (1993) *Arabidopsis* ethylene-response gene ETR1: similarity of product to two-component regulators. *Science* **262,** 539–544
9. Gamble, R. L., Coonfield, M. L., and Schaller, G. E. (1998) Histidine kinase activity of the ETR1 ethylene receptor from *Arabidopsis*. *Proc. Natl. Acad. Sci. U.S.A.* **95,** 7825–7829
10. Moussatche, P., and Klee, H. J. (2004) Autophosphorylation activity of the *Arabidopsis* ethylene receptor multigene family. *J. Biol. Chem.* **279,** 48734–48741
11. Gamble, R. L., Qu, X., and Schaller, G. E. (2002) Mutational analysis of the ethylene receptor ETR1. Role of the histidine kinase domain in dominant ethylene insensitivity. *Plant Physiol.* **128,** 1428–1438
12. Hua, J., and Meyerowitz, E. M. (1998) Ethylene responses are negatively regulated by a receptor gene family in *Arabidopsis thaliana*. *Cell* **94,** 261–271
13. McDaniel, B. K., and Binder, B. M. (2012) Ethylene receptor 1 (ETR1) is sufficient and has the predominant role in mediating inhibition of ethylene responses by silver in *Arabidopsis thaliana*. *J. Biol. Chem.* **287,** 26094–26103
14. Casino, P., Rubio, V., and Marina, A. (2009) Structural insight into partner specificity and phosphoryl transfer in two-component signal transduction. *Cell* **139,** 325–336
15. Wang, C., Sang, J., Wang, J., Su, M., Downey, J. S., Wu, Q., Wang, S., Cai,

Y., Xu, X., Wu, J., Senadheera, D. B., Cvitkovitch, D. G., Chen, L., Goodman, S. D., and Han, A. (2013) Mechanistic insights revealed by the crystal structure of a histidine kinase with signal transducer and sensor domains. *PLoS Biol.* **11,** e1001493
16. Albanesi, D., Martín, M., Trajtenberg, F., Mansilla, M. C., Haouz, A., Alzari, P. M., de Mendoza, D., and Buschiazzo, A. (2009) Structural plasticity and catalysis regulation of a thermosensor histidine kinase. *Proc. Natl. Acad. Sci.* **106,** 16185–16190
17. Ferris, H. U., Dunin-Horkawicz, S., Hornig, N., Hulko, M., Martin, J., Schultz, J. E., Zeth, K., Lupas, A. N., and Coles, M. (2012) Mechanism of regulation of receptor histidine kinases. *Structure* **20,** 56–66
18. Huang, Y., Li, H., Hutchison, C. E., Laskey, J., and Kieber, J. J. (2003) Biochemical and functional analysis of CTR1, a protein kinase that negatively regulates ethylene signaling in *Arabidopsis*. *Plant J.* **33,** 221–233
19. Gao, Z., Chen, Y.-F., Randlett, M. D., Zhao, X.-C., Findell, J. L., Kieber, J. J., and Schaller, G. E. (2003) Localization of the Raf-like kinase CTR1 to the endoplasmic reticulum of *Arabidopsis* through participation in ethylene receptor signaling complexes. *J. Biol. Chem.* **278,** 34725–34732
20. Clark, K. L., Larsen, P. B., Wang, X., and Chang, C. (1998) Association of the *Arabidopsis* CTR1 Raf-like kinase with the ETR1 and ERS ethylene receptors. *Proc. Natl. Acad. Sci. U.S.A.* **95,** 5401–5406
21. Kieber, J. J., Rothenberg, M., Roman, G., Feldmann, K. A., and Ecker, J. R. (1993) CTR1, a negative regulator of the ethylene response pathway in *Arabidopsis*, encodes a member of the raf family of protein kinases. *Cell* **72,** 427–441
22. Zhao, Q., and Guo, H.-W. (2011) Paradigms and paradox in the ethylene signaling pathway and interaction network. *Mol. Plant* **4,** 626–634
23. Hahn, A., and Harter, K. (2009) Mitogen-activated protein kinase cascades and ethylene: signaling, biosynthesis, or both? *Plant Physiol.* **149,** 1207–1210
24. Ju, C., Yoon, G. M., Shemansky, J. M., Lin, D. Y., Ying, Z. I., Chang, J., Garrett, W. M., Kessenbrock, M., Groth, G., Tucker, M. L., Cooper, B., Kieber, J. J., and Chang, C. (2012) CTR1 phosphorylates the central regulator EIN2 to control ethylene hormone signaling from the ER membrane to the nucleus in *Arabidopsis*. *Proc. Natl. Acad. Sci. U.S.A.* **109,** 19486–19491
25. Qiao, H., Shen, Z., Huang, S.-S., Schmitz, R. J., Urich, M. A., Briggs, S. P., and Ecker, J. R. (2012) Processing and subcellular trafficking of ER-tethered EIN2 control response to ethylene gas. *Science* **338,** 390–393
26. Qu, X., Hall, B. P., Gao, Z., and Schaller, G. E. (2007) A strong constitutive ethylene-response phenotype conferred on *Arabidopsis* plants containing null mutations in the ethylene receptors ETR1 and ERS1. *BMC Plant Biol.* **7,** 3
27. Gao, Z., Wen, C.-K., Binder, B. M., Chen, Y.-F., Chang, J., Chiang, Y.-H., Kerris, R. J., 3rd, Chang, C., and Schaller, G. E. (2008) Heteromeric interactions among ethylene receptors mediate signaling in *Arabidopsis*. *J. Biol. Chem.* **283,** 23801–23810
28. Mayerhofer, H., Panneerselvam, S., and Mueller-Dieckmann, J. (2012) Protein kinase domain of CTR1 from *Arabidopsis thaliana* promotes ethylene receptor cross talk. *J. Mol. Biol.* **415,** 768–779
29. Qiu, L., Xie, F., Yu, J., and Wen, C.-K. (2012) *Arabidopsis* RTE1 is essential to ethylene receptor ETR1 amino-terminal signaling independent of CTR1. *Plant Physiol.* **159,** 1263–1276
30. Wagner, J. R., Zhang, J., Brunzelle, J. S., Vierstra, R. D., and Forest, K. T. (2007) High resolution structure of *Deinococcus* bacteriophytochrome yields new insights into phytochrome architecture and evolution. *J. Biol. Chem.* **282,** 12298–12309
31. Müller-Dieckmann, H. J., Grantz, A. A., and Kim, S. H. (1999) The structure of the signal receiver domain of the *Arabidopsis thaliana* ethylene receptor ETR1. *Structure* **7,** 1547–1556
32. Zhou, P., Lugovskoy, A. A., and Wagner, G. (2001) A solubility-enhancement tag (SET) for NMR studies of poorly behaving proteins. *J. Biomol. NMR* **20,** 11–14
33. Mayerhofer, H., and Mueller-Dieckmann, J. (2013) Cloning, expression, purification and preliminary x-ray analysis of the dimerization domain of ethylene response sensor 1 (ERS1) from *Arabidopsis thaliana*. *Acta Crystallogr. Sect. F Struct. Biol. Cryst. Commun.* **69,** 1029–1032
34. Kabsch, W. (2010) XDS. *Acta Crystallogr. D Biol. Crystallogr.* **66,** 125–132
35. Collaborative Computational Project, Number 4 (1994) The CCP4 suite: programs for protein crystallography. *Acta Crystallogr. D Biol Crystallogr.* **50,** 760–763
36. Evans, P. (2006) Scaling and assessment of data quality. *Acta Crystallogr. D Biol. Crystallogr.* **62,** 72–82
37. Pape, T., and Schneider, T. R. (2004) HKL2MAP: a graphical user interface for macromolecular phasing with SHELX programs. *J. Appl. Crystallogr.* **37,** 843–844
38. Langer, G., Cohen, S. X., Lamzin, V. S., and Perrakis, A. (2008) Automated macromolecular model building for x-ray crystallography using ARP/wARP version 7. *Nat. Protoc.* **3,** 1171–1179
39. Adams, P. D., Afonine, P. V., Bunkóczi, G., Chen, V. B., Davis, I. W., Echols, N., Headd, J. J., Hung, L.-W., Kapral, G. J., Grosse-Kunstleve, R. W., McCoy, A. J., Moriarty, N. W., Oeffner, R., Read, R. J., Richardson, D. C., Richardson, J. S., Terwilliger, T. C., and Zwart, P. H. (2010) PHENIX: a comprehensive Python-based system for macromolecular structure solution. *Acta Crystallogr. D Biol. Crystallogr.* **66,** 213–221
40. Emsley, P., Lohkamp, B., Scott, W. G., and Cowtan, K. (2010) Features and development of Coot. *Acta Crystallogr. D Biol. Crystallogr.* **66,** 486–501
41. Chen, V. B., Arendall, W. B., 3rd, Headd, J. J., Keedy, D. A., Immormino, R. M., Kapral, G. J., Murray, L. W., Richardson, J. S., and Richardson, D. C. (2010) MolProbity: all-atom structure validation for macromolecular crystallography. *Acta Crystallogr. D Biol. Crystallogr.* **66,** 12–21
42. Panneerselvam, S., Kaljunen, H., and Mueller-Dieckmann, J. (2013) Cloning, overexpression, purification and preliminary x-ray analysis of the catalytic domain of the ethylene receptor ETR1 from *Arabidopsis thaliana*. *Acta Crystallogr. Sect. F Struct. Biol. Cryst. Commun.* **69,** 1307–1309
43. Panjikar, S., Parthasarathy, V., Lamzin, V. S., Weiss, M. S., and Tucker, P. A. (2005) Auto-Rickshaw: an automated crystal structure determination platform as an efficient tool for the validation of an x-ray diffraction experiment. *Acta Crystallogr. D Biol. Crystallogr.* **61,** 449–457
44. Sheldrick, G. M. (2008) A short history of SHELX. *Acta Crystallogr. A* **64,** 112–122
45. Roessle, M. W., Klaering, R., Ristau, U., Robrahn, B., Jahn, D., Gehrmann, P., Konarev, P., Round, A., Fiedler, S., Hermes, C., and Svergun, D. (2007) Upgrade of the small-angle x-ray scattering beamline X33 at the European Molecular Biology Laboratory, Hamburg. *J. Appl. Crystallogr.* **40,** 190–194
46. Konarev, P. V., Volkov, V. V., Sokolova, A. V., Koch, M. H., and Svergun, D. I. (2003) PRIMUS: a Windows PC-based system for small-angle scattering data analysis. *J. Appl. Crystallogr.* **36,** 1277–1282
47. Guinier, A. (1939) La diffraction des rayons x aux tres petits angles; application a l'etude de phenomenes ultramicroscopiques. *Ann. Phys.* **12,** 161–237
48. Svergun, D. I. (1992) Determination of the regularization parameter in indirect-transform methods using perceptual criteria. *J. Appl. Crystallogr.* **25,** 495–503
49. Petoukhov, M. V., Franke, D., Shkumatov, A. V., Tria, G., Kikhney, A. G., Gajda, M., Gorba, C., Mertens, H. D. T., Konarev, P. V., and Svergun, D. I. (2012) New developments in the ATSAS program package for small-angle scattering data analysis. *J. Appl. Crystallogr.* **45,** 342–350
50. Svergun, D., Barberato, C., and Koch, M. H. J. (1995) CRYSOL—a program to evaluate x-ray solution scattering of biological macromolecules from atomic coordinates. *J. Appl. Crystallogr.* **28,** 768–773
51. Franke, D., and Svergun, D. I. (2009) DAMMIF, a program for rapid *ab initio* shape determination in small-angle scattering. *J. Appl. Crystallogr.* **42,** 342–346
52. Svergun, D. I. (1999) Restoring low resolution structure of biological macromolecules from solution scattering using simulated annealing. *Biophys. J.* **76,** 2879–2886
53. Volkov, V. V., and Svergun, D. I. (2003) Uniqueness of *ab initio* shape determination in small-angle scattering. *J. Appl. Crystallogr.* **36,** 860–864
54. Petoukhov, M. V., and Svergun, D. I. (2005) Global rigid body modeling of macromolecular complexes against small-angle scattering data. *Biophys. J.* **89,** 1237–1250
55. Kozin, M. B., and Svergun, D. I. (2001) Automated matching of high- and low-resolution structural models. *J. Appl. Crystallogr.* **34,** 33–41
56. Eswar, N., Webb, B., Marti-Renom, M. A., Madhusudhan, M. S., Eramian,

D., Shen, M., Pieper, U., and Sali, A. (2002) *Current Protocols in Bioinformatics*, John Wiley & Sons, Inc., New York
57. Ulijasz, A. T., Cornilescu, G., Cornilescu, C. C., Zhang, J., Rivera, M., Markley, J. L., and Vierstra, R. D. (2010) Structural basis for the photoconversion of a phytochrome to the activated Pfr form. *Nature* **463,** 250–254
58. Martinez, S. E., Wu, A. Y., Glavas, N. A., Tang, X.-B., Turley, S., Hol, W. G., and Beavo, J. A. (2002) The two GAF domains in phosphodiesterase 2A have distinct roles in dimerization and in cGMP binding. *Proc. Natl. Acad. Sci. U.S.A.* **99,** 13260–13265
59. Bernadó, P., Mylonas, E., Petoukhov, M. V., Blackledge, M., and Svergun, D. I. (2007) Structural characterization of flexible proteins using small-angle x-ray scattering. *J. Am. Chem. Soc.* **129,** 5656–5664
60. Marina, A., Mott, C., Auyzenberg, A., Hendrickson, W. A., and Waldburger, C. D. (2001) Structural and mutational analysis of the PhoQ histidine kinase catalytic domain. *J. Biol. Chem.* **276,** 41182–41190
61. Bilwes, A. M., Quezada, C. M., Croal, L. R., Crane, B. R., and Simon, M. I. (2001) Nucleotide binding by the histidine kinase CheA. *Nat. Struct. Biol.* **8,** 353–360
62. Yamada, S., Sugimoto, H., Kobayashi, M., Ohno, A., Nakamura, H., and Shiro, Y. (2009) Structure of PAS-linked histidine kinase and the response regulator complex. *Structure* **17,** 1333–1344
63. Dunin-Horkawicz, S., and Lupas, A. N. (2010) Measuring the conformational space of square four-helical bundles with the program samCC. *J. Struct. Biol.* **170,** 226–235
64. Yang, Y., and Inouye, M. (1991) Intermolecular complementation between two defective mutant signal-transducing receptors of *Escherichia coli*. *Proc. Natl. Acad. Sci. U.S.A.* **88,** 11057–11061
65. Petoukhov, M. V., Konarev, P. V., Kikhney, A. G., and Svergun, D. I. (2007) ATSAS 2.1—towards automated and web-supported small-angle scattering data analysis. *J. Appl. Crystallogr.* **40,** 223–228

Structural Model of the Cytosolic Domain of the Plant Ethylene Receptor 1 (ETR1)

Hubert Mayerhofer, Saravanan Panneerselvam, Heidi Kaljunen, Anne Tuukkanen, Haydyn D. T. Mertens and Jochen Mueller-Dieckmann

J. Biol. Chem. 2015, 290:2644-2658.
doi: 10.1074/jbc.M114.587667 originally published online December 1, 2014
